

The Bispectrum as a Signature of Gravitational Instability in Redshift-Space

Román Scoccimarro¹, H. M. P. Couchman², and Joshua A. Frieman^{3,4}

¹CITA, McLennan Physical Labs, 60 St George Street, Toronto, ON M5S 3H8, Canada

²Department of Physics and Astronomy, University of Western Ontario, London,
ON N6A 3K7, Canada

³NASA/Fermilab Astrophysics Center, Fermi National Accelerator Laboratory,
P.O. Box 500, Batavia, IL 60510

⁴Department of Astronomy and Astrophysics, University of Chicago, Chicago, IL 60637

ABSTRACT

The bispectrum provides a characteristic signature of gravitational instability that can be used to probe the Gaussianity of the initial conditions and the bias of the galaxy distribution. We study how this signature is affected by redshift distortions using perturbation theory and high-resolution numerical simulations. We obtain perturbative results for the multipole expansion of the redshift-space bispectrum which provide a natural way to break the degeneracy between bias and Ω present in measurements of the redshift-space power spectrum. We propose a phenomenological model that incorporates the perturbative results and also describes the bispectrum in the transition to the non-linear regime. We stress the importance of non-linear effects and show that inaccurate treatment of these can lead to significant discrepancies in the determination of bias from galaxy redshift surveys. At small scales we find that the bispectrum monopole exhibits a strong configuration dependence that reflects the velocity dispersion of clusters. Therefore, the hierarchical model for the three-point function does not hold in redshift-space.

Subject headings: large-scale structure of universe; methods: numerical; methods: statistical

1. Introduction

Understanding the origin of the large-scale distribution of galaxies in the Universe remains a fundamental goal of cosmology. Galaxy redshift surveys provide a unique resource for this endeavor. Recession velocities, however, are not exact indicators of galaxy radial distances, since gravitational instability induces peculiar velocities which contribute to galaxy redshifts. This departure from the Hubble flow causes the observed clustering distribution in redshift surveys to be statistically anisotropic. On large scales, the clustering pattern is compressed along the line-of-sight (the “squashing effect”) by coherent infall onto galaxy clusters and superclusters and outflow from voids and other underdense regions (Sargent & Turner 1977). On small scales, the velocity dispersion of virialized clusters creates the so-called “fingers of god” (FOG) by stretching out these structures along the line-of-sight (Jackson 1972). The anisotropy of galaxy redshift-space clustering provides valuable information about the galaxy velocity field and hence the underlying mass density field. In particular, measurements of redshift-space distortions can be used to determine the matter density parameter Ω .

Modelling the redshift distortions of clustering statistics is a prerequisite for extracting information from redshift surveys (see Hamilton 1997 for a review). The effects of redshift distortions are well understood in linear perturbation theory: galaxy power spectrum measurements on large scales can be used to determine the combination $\beta \equiv \Omega^{0.6}/b$, where b is the linear bias factor (Kaiser 1987, Hamilton 1992). This degeneracy between bias and Ω can be lifted in principle by using higher-order statistics, such as the bispectrum, to independently constrain b (Fry & Gaztañaga 1993; Fry 1994; Gaztañaga & Frieman 1994; Matarrese, Verde & Heavens 1997). However, to apply this technique to redshift surveys, redshift distortions of the bispectrum must be taken into account as well. Hivon et al. (1995) used second-order Lagrangian perturbation theory to calculate redshift distortions of the bispectrum monopole, and found them to be rather small, at most 10%. In this paper, we compute the redshift distortions in Eulerian perturbation theory and extend their results to the bispectrum quadrupole. The latter contains valuable information about Ω , which complements that encoded in the power spectrum distortions.

As has become evident in recent years from comparisons with numerical simulations, leading-order perturbative calculations—such as linear theory for the power spectrum—break down at larger scales in redshift space than in real space. In this work, we find a similar result for the bispectrum. Moreover, mildly non-linear effects are inevitably present in observations and must be adequately taken into account to take full advantage of the data (Cole, Fisher & Weinberg 1994, 1995; Hatton & Cole 1998). In particular, the next generation of galaxy redshift surveys, such as the Two Degree Field and Sloan Digital Sky Surveys, will provide their most precise measurements of redshift distortions on intermediate scales, where non-linear effects cannot be neglected. In order to improve upon the perturbative description of the redshift-space bispectrum, we develop a simple phenomenological model that extends the perturbative results to smaller scales, analogous to what has been done for the power spectrum multipoles. We compare our results with numerical simulations and find very good agreement even well into the non-linear regime. We find that the reduced redshift-space bispectrum Q_s maintains its configuration dependence at all scales (in contrast to what happens in real space), due to anisotropies arising from the velocity dispersion along the line-of-sight. This effect, if not included, would otherwise compromise the program to use the configuration dependence of the bispectrum to constrain the bias from measurements in redshift surveys.

The rest of this paper is organized as follows. In Section 2, we derive a fully non-linear expression for the density field in redshift space, which is then used to obtain the perturbative expansion order by order. Section 3 applies these results to yield the monopole and quadrupole moments of the redshift-space

bispectrum for different configurations, including non-linear biasing. The extension of these results into the non-linear regime via a phenomenological model is the subject of Section 4, where comparison with numerical simulations is made. Section 5 provides a final discussion and conclusions.

2. Redshift-Space Mapping and Perturbation Theory

In redshift space, the radial coordinate \mathbf{s} of a galaxy is given by its observed radial velocity, a combination of its Hubble flow plus “distortions” due to peculiar velocities. The mapping from real-space position \mathbf{x} to redshift space is given by:

$$\mathbf{s} = \mathbf{x} - f u_z(\mathbf{x}) \hat{z}, \quad (1)$$

where $f(\Omega) \approx \Omega^{0.6}$ is the logarithmic growth rate of linear perturbations, and $\mathbf{u}(\mathbf{x}) \equiv -\mathbf{v}(\mathbf{x})/(\mathcal{H}f)$, where $\mathbf{v}(\mathbf{x})$ is the peculiar velocity field, and $\mathcal{H}(\tau) \equiv (1/a)(da/d\tau) = Ha$ is the conformal Hubble parameter (with FRW scale factor $a(\tau)$ and conformal time τ). In Eq. (1), we have assumed the “plane-parallel” (or infinitely remote observer) approximation, so that the line-of-sight is taken as a fixed direction, denoted by \hat{z} .

The density field in redshift space, $\delta_s(\mathbf{s})$, is obtained from the real-space density field $\delta(\mathbf{x})$ by requiring that the redshift-space mapping conserves the number of galaxies, i.e.

$$(1 + \delta_s)d^3s = (1 + \delta)d^3x. \quad (2)$$

Using the fact that $d^3s = J(\mathbf{x})d^3x$, where $J(\mathbf{x}) = 1 - f\nabla_z u_z(\mathbf{x})$ is the *exact* Jacobian of the mapping in the plane-parallel approximation, we obtain:

$$\delta_s(\mathbf{s}) = \frac{\delta(\mathbf{x}) + 1 - J(\mathbf{x})}{J(\mathbf{x})} = \frac{\delta(\mathbf{x}) + f\nabla_z u_z(\mathbf{x})}{1 - f\nabla_z u_z(\mathbf{x})}. \quad (3)$$

The zeros of the Jacobian describe caustics in redshift space, the locus of points where the density field is apparently infinite (McGill 1990). This surface is characterized in real space by those points which are undergoing turn-around in the gravitational collapse process, so their peculiar velocities exactly cancel the differential Hubble flow. In practice, caustics are smoothed out by subclustering.

We are interested in the Fourier transform of the density field contrast in redshift space,

$$\delta_s(\mathbf{k}) \equiv \int \frac{d^3s}{(2\pi)^3} e^{-i\mathbf{k}\cdot\mathbf{s}} \delta_s(\mathbf{s}) = \int \frac{d^3x}{(2\pi)^3} e^{-i\mathbf{k}\cdot\mathbf{x}} e^{ifk_z u_z(\mathbf{x})} \left[\delta(\mathbf{x}) + f\nabla_z u_z(\mathbf{x}) \right]. \quad (4)$$

This equation describes the fully non-linear density field in redshift space in the plane-parallel approximation and is the starting point for the perturbative approach. The term in square brackets describes the “squashing effect”, *i.e.*, the increase in the clustering amplitude due to infall, whereas the exponential factor encodes the FOG effect, which erases power due to velocity dispersion along the line-of-sight. To obtain the perturbative expansion, we expand the second exponential in power series,

$$\delta_s(\mathbf{k}) = \sum_{n=1}^{\infty} \int d^3k_1 \dots d^3k_n [\delta_{\mathbf{D}}]_n \left[\delta(\mathbf{k}_1) + f\mu_1^2 \theta(\mathbf{k}_1) \right] \frac{(f\mu k)^{n-1}}{(n-1)!} \frac{\mu_2}{k_2} \theta(\mathbf{k}_2) \dots \frac{\mu_n}{k_n} \theta(\mathbf{k}_n), \quad (5)$$

where $[\delta_{\mathbf{D}}]_n \equiv \delta_{\mathbf{D}}(\mathbf{k} - \mathbf{k}_1 - \dots - \mathbf{k}_n)$, with $\delta_{\mathbf{D}}(\mathbf{x})$ the Dirac delta distribution, the velocity divergence $\theta(\mathbf{x}) \equiv \nabla \cdot \mathbf{u}(\mathbf{x})$, and $\mu_i \equiv \mathbf{k}_i \cdot \hat{z}/k_i$ is the cosine of the angle between the line-of-sight and the wavevector.

In linear perturbation theory, only the $n = 1$ term survives, and we recover the well known formula due to Kaiser (1987)

$$\delta_s(\mathbf{k}) = \delta(\mathbf{k})(1 + f\mu^2). \quad (6)$$

Equation (5) can be used to obtain the redshift-space density field beyond linear theory. For this purpose, we recall that the perturbative expansion for the *un-redshifted* density and velocity-divergence fields can be written (Fry 1984, Goroff et al. 1986)

$$\delta(\mathbf{k}, \tau) = \sum_{n=1}^{\infty} D_1^n(\tau) \int d^3k_1 \dots \int d^3k_n [\delta_D]_n F_n(\mathbf{k}_1, \dots, \mathbf{k}_n) \delta_1(\mathbf{k}_1) \dots \delta_1(\mathbf{k}_n), \quad (7)$$

$$\theta(\mathbf{k}, \tau) = \sum_{n=1}^{\infty} D_1^n(\tau) \int d^3k_1 \dots \int d^3k_n [\delta_D]_n G_n(\mathbf{k}_1, \dots, \mathbf{k}_n) \delta_1(\mathbf{k}_1) \dots \delta_1(\mathbf{k}_n), \quad (8)$$

where $D_1(\tau)$ is the density perturbation growth factor in linear theory. Here we have assumed that the n^{th} -order growth factor $D_n \propto D_1^n$, which is an excellent approximation (see Scoccimarro et al. 1998, Appendix B.3). The perturbative kernels F_n and G_n are dimensionless, symmetric, scalar functions of the wave vectors $\{\mathbf{k}_1, \dots, \mathbf{k}_n\}$ which can be recursively found from the equations of motion. Similarly, in redshift space we can write the density field amplitude in the form

$$\delta_s(\mathbf{k}, \tau) = \sum_{n=1}^{\infty} D_1^n(\tau) \int d^3k_1 \dots \int d^3k_n [\delta_D]_n Z_n(\mathbf{k}_1, \dots, \mathbf{k}_n) \delta_1(\mathbf{k}_1) \dots \delta_1(\mathbf{k}_n). \quad (9)$$

To proceed, we assume a local, non-linear biasing scheme, in which the galaxy density contrast δ_g is given as a Taylor series expansion in the underlying dark matter fluctuations δ (Fry & Gaztañaga 1993),

$$\delta_g = \sum_{m=0}^{\infty} \frac{b_m}{m!} \delta^m \equiv b (\delta + \gamma\delta^2/2 + \dots), \quad (10)$$

where $\gamma = b_2/b$, and $b \equiv b_1$ is the linear bias. If the galaxy distribution is unbiased, then $b = 1$ and $b_m = 0$ for $m > 1$. The term b_0 ensures that $\langle \delta_g \rangle = 0$; since it does not enter into connected correlations, we will neglect it in what follows, as assumed in the last expression in Eq. (10). We note that the model in Eq. (10) is a rather simple bias prescription, and one could generalize the results below to more complex biasing schemes (e.g., non-local, time-dependent, stochastic, etc).

From Eqs. (5)-(10), we can now read off the redshift-space kernels Z_n for the *galaxy* density field. In particular the linear, second- and third-order perturbation theory (PT) kernels are

$$Z_1(\mathbf{k}) = (b + f\mu^2), \quad (11)$$

$$Z_2(\mathbf{k}_1, \mathbf{k}_2) = bF_2(\mathbf{k}_1, \mathbf{k}_2) + f\mu^2 G_2(\mathbf{k}_1, \mathbf{k}_2) + \frac{f\mu k}{2} \left[\frac{\mu_1}{k_1} (b + f\mu_2^2) + \frac{\mu_2}{k_2} (b + f\mu_1^2) \right] + \frac{b_2}{2}, \quad (12)$$

$$\begin{aligned} Z_3(\mathbf{k}_1, \mathbf{k}_2, \mathbf{k}_3) &= bF_3^{(s)}(\mathbf{k}_1, \mathbf{k}_2, \mathbf{k}_3) + f\mu^2 G_3^{(s)}(\mathbf{k}_1, \mathbf{k}_2, \mathbf{k}_3) + f\mu k \left[bF_2^{(s)}(\mathbf{k}_1, \mathbf{k}_2) + f\mu_{12}^2 G_2^{(s)}(\mathbf{k}_1, \mathbf{k}_2) \right] \frac{\mu_3}{k_3} \\ &\quad + f\mu k (b + f\mu_1^2) \frac{\mu_{23}}{k_{23}} G_2^{(s)}(\mathbf{k}_2, \mathbf{k}_3) + \frac{(f\mu k)^2}{2} (b + f\mu_1^2) \frac{\mu_2}{k_2} \frac{\mu_3}{k_3} + 3b_2 F_2^{(s)}(\mathbf{k}_1, \mathbf{k}_2) + \frac{b_3}{6}, \end{aligned} \quad (13)$$

where we denote $\mu \equiv \mathbf{k} \cdot \hat{z}/k$, with $\mathbf{k} \equiv \mathbf{k}_1 + \dots + \mathbf{k}_n$, and $\mu_i \equiv \mathbf{k}_i \cdot \hat{z}/k_i$. As above, F_2 and G_2 (given in Eqs. (22-23) below) denote the second-order kernels for the real-space density and velocity-divergence fields, and similarly for F_3 and G_3 . Note that the third order kernel Z_3 must still be symmetrized over its arguments. One can similarly obtain the PT kernels Z_n in redshift space to arbitrary higher order.

We note that there are *two* approximations involved in this procedure: one is the mathematical step of going from Eq. (4) to Eq. (5), which approximates the redshift-space mapping with a power series; the other is the PT expansion itself (i.e., the expansion of $\delta(\mathbf{k})$ and $\theta(\mathbf{k})$ in terms of linear fluctuations $\delta_1(\mathbf{k})$). Therefore, one is not guaranteed that the resulting PT in redshift space will work over the same range of scales as in real space. In fact, we will find that, in general, *PT in redshift space breaks down at larger scales than in real space*, because the redshift-space mapping is only treated approximately, and it breaks down at larger scales than does the perturbative dynamics. In particular, a calculation of the one-loop power spectrum in redshift space using Eqs. (11-13) does not give satisfactory results. To extend the leading-order calculations such as those in this work, one must treat the redshift-space mapping exactly and only approximate the dynamics using PT (Scoccimarro, Couchman & Frieman 1998; hereafter SCF).

The calculation of redshift-space statistics in Fourier space proceeds along the same lines as in the un-redshifted case. To leading (linear) order, the redshift-space galaxy power spectrum reads (Kaiser 1987)

$$P_s(\mathbf{k}) = P_g(k) (1 + \beta\mu^2)^2 = \sum_{\ell=0}^{\infty} a_\ell P_\ell(\mu) P_g(k), \quad (14)$$

where $P_g(k) \equiv b^2 P(k)$ is the real-space galaxy power spectrum, $P(k)$ is the linear mass power spectrum, and $\beta \equiv f/b \approx \Omega^{0.6}/b$. Here $P_\ell(\mu)$ denotes the Legendre polynomial of order ℓ , and the multipole coefficients are (Hamilton 1992; Cole, Fisher & Weinberg 1994)

$$a_0 \equiv 1 + \frac{2}{3}\beta + \frac{1}{5}\beta^2, \quad a_2 \equiv \frac{4}{3}\beta + \frac{4}{7}\beta^2, \quad a_4 \equiv \frac{8}{35}\beta^2; \quad (15)$$

all other multipoles vanish. Equation (14) is the standard tool for measuring Ω from redshift distortions of the power spectrum in the linear regime; in particular, the quadrupole-to-monopole ratio $R_P \equiv a_2/a_0$ should be a constant, independent of wavevector k , as $k \rightarrow 0$. Note, however, that in these expressions Ω appears only through the parameter β , so there is a degeneracy between Ω and the linear bias factor b (it is impossible to distinguish an unbiased low-density Universe from a biased high-density model).

Given the second-order PT kernel in redshift-space, the leading-order (tree-level) galaxy bispectrum in redshift-space reads

$$B_s(\mathbf{k}_1, \mathbf{k}_2, \mathbf{k}_3) = 2Z_2(\mathbf{k}_1, \mathbf{k}_2) Z_1(\mathbf{k}_1) Z_1(\mathbf{k}_2) P(k_1) P(k_2) + \text{cyc.}, \quad (16)$$

which can be normalized by the power spectrum monopole to give the hierarchical three-point amplitude in redshift space, Q_s ,

$$Q_s(\mathbf{k}_1, \mathbf{k}_2, \mathbf{k}_3) \equiv \frac{B_s(\mathbf{k}_1, \mathbf{k}_2, \mathbf{k}_3)}{P_s(k_1) P_s(k_2) + \text{cyc.}} = \frac{B_s(\mathbf{k}_1, \mathbf{k}_2, \mathbf{k}_3)}{a_0^2 (P_g(k_1) P_g(k_2) + \text{cyc.})}, \quad (17)$$

where ‘‘cyc.’’ denotes a sum over permutations of $\{k_1, k_2, k_3\}$. Note that the hierarchical amplitude Q_s is independent of power spectrum normalization to leading order in PT. Since, to leading order, Q_s is a *function* of triangle configuration which separately depends on Ω , b , and b_2 , it allows one in principle to

break the degeneracy between Ω and b present in measurement of the power spectrum multipoles in redshift space.

3. Results: The Redshift-Space Bispectrum in Perturbation Theory

Due to redshift distortions, the bispectrum becomes a function of five variables: three of them describe the shape of the triangle (e.g., the sides k_1 , k_2 , and the angle θ between them, with $\cos \theta \equiv \hat{\mathbf{k}}_1 \cdot \hat{\mathbf{k}}_2$), and the two remaining variables characterize the orientation of the triangle with respect to the line-of-sight, which we take to be the polar angle $\omega = \cos^{-1} \mu$ of \mathbf{k}_1 , and the azimuthal angle ϕ about $\hat{\mathbf{k}}_1$:

$$\mu_1 = \mu = \cos \omega = \hat{\mathbf{k}}_1 \cdot \hat{z}, \quad \mu_2 = \mu \cos \theta - \sqrt{(1 - \mu^2)} \sin \theta \cos \phi, \quad \mu_3 = -\frac{k_1}{k_3} \mu - \frac{k_2}{k_3} \mu_2. \quad (18)$$

The (μ, ϕ) dependence introduced by redshift distortions can be conveniently described by decomposing the tree-level bispectrum B_s in Eq. (16) into spherical harmonics,

$$B_s(\mathbf{k}_1, \mathbf{k}_2, \mathbf{k}_3) = \sum_{\ell=0}^{\infty} \sum_{m=-\ell}^{\ell} B_s^{(\ell, m)}(k_1, k_2, \theta) Y_{\ell m}(\omega, \phi). \quad (19)$$

Bispectrum multipoles $B_s^{(\ell, m)}$ are non-vanishing for even ℓ , up to $\ell = 8$, $m = 6$. We now explore the information encoded in these multipoles for different triangle configurations.

3.1. Non-Equilateral Configurations

Rather than working with the full multipole decomposition (ℓ, m) , here we concentrate for simplicity on the $m = 0$ multipoles. In this case, which corresponds to averaging over ϕ , it is more convenient to decompose the bispectrum in Legendre polynomials

$$B_s(\mathbf{k}_1, \mathbf{k}_2, \mathbf{k}_3) = \sum_{\ell=0}^{\infty} B_s^{(\ell)}(k_1, k_2, \theta) P_{\ell}(\mu). \quad (20)$$

We can write the different contributions as

$$B_s^{(\ell)} = P_g(k_1)P_g(k_2) \left(F_2(\mathbf{k}_1, \mathbf{k}_2) \mathcal{D}_{\text{SQ1}}^{\ell} + G_2(\mathbf{k}_1, \mathbf{k}_2) \mathcal{D}_{\text{SQ2}}^{\ell} + \mathcal{D}_{\text{NLB}}^{\ell} + \mathcal{D}_{\text{FOG}}^{\ell} \right) + \text{cyc.}, \quad (21)$$

where the second-order real-space kernels are given by

$$F_2(\mathbf{k}_1, \mathbf{k}_2) = \frac{5}{7} + \frac{x}{2} \left(\frac{k_1}{k_2} + \frac{k_2}{k_1} \right) + \frac{2x^2}{7}, \quad (22)$$

$$G_2(\mathbf{k}_1, \mathbf{k}_2) = \frac{3}{7} + \frac{x}{2} \left(\frac{k_1}{k_2} + \frac{k_2}{k_1} \right) + \frac{4x^2}{7}, \quad (23)$$

with $x \equiv \cos \theta$. The first term in Eq. (21) represents the effect of the linear squashing (SQ1), the next term describes second-order squashing (SQ2), the third contribution is due to non-linear biasing (NLB),

and the last term describes the effect of damping due to velocity dispersion, the FOG effect. The different contributions to the monopole ($\ell = 0$) and quadrupole ($\ell = 2$) are given by (recall that $\beta \equiv f/b$, $\gamma = b_2/b$)

$$\mathcal{D}_{\text{SQ1}}^{\ell=0} \equiv \frac{2 (15 + 10\beta + \beta^2 + 2\beta^2 x^2)}{15b}, \quad (24)$$

$$\mathcal{D}_{\text{SQ1}}^{\ell=2} \equiv \frac{2\beta (7 + \beta + 21x^2 + 11\beta x^2)}{21b}, \quad (25)$$

$$\begin{aligned} \mathcal{D}_{\text{SQ2}}^{\ell=0} \equiv & 2\beta (35k_1^2 + 28\beta k_1^2 + 3\beta^2 k_1^2 + 35k_2^2 + 28\beta k_2^2 + 3\beta^2 k_2^2 + 70k_1 k_2 x + 84\beta k_1 k_2 x + \\ & 18\beta^2 k_1 k_2 x + 14\beta k_1^2 x^2 + 12\beta^2 k_1^2 x^2 + 14\beta k_2^2 x^2 + 12\beta^2 k_2^2 x^2 + 12\beta^2 k_1 k_2 x^3) \\ & / (105k_3^2 b) \end{aligned} \quad (26)$$

$$\begin{aligned} \mathcal{D}_{\text{SQ2}}^{\ell=2} \equiv & 2\beta (14k_1^2 + 13\beta k_1^2 + \beta^2 k_1^2 - 7k_2^2 - 5\beta k_2^2 + 28k_1 k_2 x + 30\beta k_1 k_2 x + 6\beta^2 k_1 k_2 x + \\ & 11\beta k_1^2 x^2 + 9\beta^2 k_1^2 x^2 + 21k_2^2 x^2 + 29\beta k_2^2 x^2 + 6\beta^2 k_2^2 x^2 + 18\beta k_1 k_2 x^3 + 14\beta^2 k_1 k_2 x^3 + \\ & 4\beta^2 k_2^2 x^4) / (21k_3^2 b) \end{aligned} \quad (27)$$

$$\mathcal{D}_{\text{NLB}}^{\ell=0} \equiv \frac{\gamma (15 + 10\beta + \beta^2 + 2\beta^2 x^2)}{15b} \quad (28)$$

$$\mathcal{D}_{\text{NLB}}^{\ell=2} \equiv \frac{\beta\gamma (7 + \beta + 21x^2 + 11\beta x^2)}{21b} \quad (29)$$

$$\begin{aligned} \mathcal{D}_{\text{FOG}}^{\ell=0} \equiv & \beta (210k_1 k_2 + 210\beta k_1 k_2 + 54\beta^2 k_1 k_2 + 6\beta^3 k_1 k_2 + 105k_1^2 x + 189\beta k_1^2 x + 99\beta^2 k_1^2 x + \\ & 15\beta^3 k_1^2 x + 105k_2^2 x + 189\beta k_2^2 x + 99\beta^2 k_2^2 x + 15\beta^3 k_2^2 x + 168\beta k_1 k_2 x^2 + \\ & 216\beta^2 k_1 k_2 x^2 + 48\beta^3 k_1 k_2 x^2 + 36\beta^2 k_1^2 x^3 + 20\beta^3 k_1^2 x^3 + 36\beta^2 k_2^2 x^3 + 20\beta^3 k_2^2 x^3 + \\ & 16\beta^3 k_1 k_2 x^4) / (315k_1 k_2) \end{aligned} \quad (30)$$

$$\begin{aligned} \mathcal{D}_{\text{FOG}}^{\ell=2} \equiv & \beta (231k_1 k_2 + 330\beta k_1 k_2 + 99\beta^2 k_1 k_2 + 12\beta^3 k_1 k_2 + 462k_1^2 x + 891\beta k_1^2 x + 528\beta^2 k_1^2 x + \\ & 75\beta^3 k_1^2 x + 462k_2^2 x + 594\beta k_2^2 x + 198\beta^2 k_2^2 x + 30\beta^3 k_2^2 x + 693k_1 k_2 x^2 + \\ & 2046\beta k_1 k_2 x^2 + 1485\beta^2 k_1 k_2 x^2 + 276\beta^3 k_1 k_2 x^2 + 297\beta k_1^2 x^3 + 462\beta^2 k_1^2 x^3 + 205\beta^3 k_1^2 x^3 + \\ & 594\beta k_2^2 x^3 + 792\beta^2 k_2^2 x^3 + 190\beta^3 k_2^2 x^3 + 396\beta^2 k_1 k_2 x^4 + 272\beta^3 k_1 k_2 x^4 + \\ & 60\beta^3 k_2^2 x^5) / (693k_1 k_2) \end{aligned} \quad (31)$$

The result for the monopole without bias, when $b = 1$ and $\gamma = 0$, agrees with that given in Hivon et al (1995), where they also include the (extremely weak) Ω -dependence due to second-order PT growth factors (i.e., the small deviation from $D_2 \propto D_1^2$). This agreement may seem surprising, since they claim to include the radial character of redshift distortions, whereas our calculations are done in the plane-parallel approximation. In fact, although intermediate expressions in Hivon et al (1995) do preserve the radial character of redshift

distortions in the large-volume approximation [equivalent to replacing z by r in Eq. (4)], the angle averaging is done instead assuming that \mathbf{r} is a fixed direction, that is, in the plane-parallel approximation. Our results generalize theirs to include biasing; more importantly, the result for the bispectrum quadrupole is new.

Figure 1 illustrates these results. The top left panel shows the amplification of the bispectrum due to redshift-space distortions, showing the ratio $A_B^{(\ell)} \equiv B_s^{(\ell)}/B$, for $\ell = 0$ and $\ell = 2$, as a function of angle θ , for configurations with $k_1/k_2 = 2$ and scale-free initial conditions, $P(k) \propto k^n$ ($n = -2$ solid curves, and $n = 0$ dotted curves). The monopole shows a small ($\leq 20\%$) change of the bispectrum due to redshift distortions, as first shown by Hivon et al. (1995). The quadrupole, however, shows a higher amplification for co-linear configurations (near $\theta = 0, \pi$, where $\mathbf{k}_1 \parallel \mathbf{k}_2$) and a suppression at equilateral-like configurations. This is to be expected, since the quadrupole is generated solely by redshift distortions, and the dominant peculiar velocities in PT are co-linear with density gradients. The top right panel shows the bispectrum quadrupole-to-monopole ratio, $R_B \equiv B_s^{(2)}/B_s^{(0)}$ for $r = k_1/k_2 = 10, 2, 1$ (top to bottom), in $\Omega = 1$ (top set) and $\Omega = 0.3$ (bottom set) models, for $n = -2$ (solid) and $n = 0$ (dotted). As in the power spectrum case, R_B increases with Ω , and it shows the expected configuration dependence; it is relatively insensitive to the shape of the power spectrum.

The bottom right plot in Figure 1 quantifies how redshift distortions alter the relation between galaxy and matter correlations. For the local, non-linear bias model of Eq. (10), the 3-point hierarchical amplitude for galaxies satisfies $Q_g = (Q + \gamma)/b$ in the absence of redshift distortions (Fry & Gaztañaga 1993, Fry 1994). As can be seen from the different terms in Eq. (21), this simple relation no longer holds in redshift space. The solid curves show the exact PT result in redshift space, while the dotted curves correspond to (wrongly) assuming that $Q_{g,s} = (Q_s + \gamma)/b$ holds in redshift space, i.e., that the operations of bias and redshift-space mapping commute. Here we have set the linear bias to $b = 2$, the non-linear bias $\gamma = 1/2, 0, -1/2$ (from top to bottom), and show configurations with $k_1/k_2 = 2$, for a model with linear spectral index $n = -2$. We see that the assumption that bias and redshift distortions commute is accurate at about the 20% level.

3.2. Equilateral Configurations

For equilateral triangle configurations ($k_1 = k_2 = k_3$), the leading-order PT expression for the redshift-space bispectrum, $B_{s \text{ eq}}$, is

$$\begin{aligned}
 B_{s \text{ eq}}(\mu, \nu) = & [P_g(k)]^2 \left(256 + 448 \gamma + 288 \beta \mu^2 + 224 b \beta \mu^2 + 448 \beta \gamma \mu^2 + 72 \beta^2 \mu^4 + 168 b \beta^2 \mu^4 + \right. \\
 & 84 \beta^2 \gamma \mu^4 + 4 \beta^3 \mu^6 - 7 b \beta^4 \mu^8 + 288 \beta \nu^2 + 224 b \beta \nu^2 + 448 \beta \gamma \nu^2 - 288 \beta \mu^2 \nu^2 - \\
 & 224 b \beta \mu^2 \nu^2 + 144 \beta^2 \mu^2 \nu^2 + 336 b \beta^2 \mu^2 \nu^2 - 448 \beta \gamma \mu^2 \nu^2 + 168 \beta^2 \gamma \mu^2 \nu^2 - 144 \beta^2 \mu^4 \nu^2 - \\
 & 336 b \beta^2 \mu^4 \nu^2 - 24 \beta^3 \mu^4 \nu^2 - 168 \beta^2 \gamma \mu^4 \nu^2 + 24 \beta^3 \mu^6 \nu^2 + 35 b \beta^4 \mu^6 \nu^2 - 35 b \beta^4 \mu^8 \nu^2 + \\
 & 72 \beta^2 \nu^4 + 168 b \beta^2 \nu^4 + 84 \beta^2 \gamma \nu^4 - 144 \beta^2 \mu^2 \nu^4 - 336 b \beta^2 \mu^2 \nu^4 + 36 \beta^3 \mu^2 \nu^4 - \\
 & 168 \beta^2 \gamma \mu^2 \nu^4 + 72 \beta^2 \mu^4 \nu^4 + 168 b \beta^2 \mu^4 \nu^4 - 72 \beta^3 \mu^4 \nu^4 - 21 b \beta^4 \mu^4 \nu^4 + 84 \beta^2 \gamma \mu^4 \nu^4 + \\
 & 36 \beta^3 \mu^6 \nu^4 + 42 b \beta^4 \mu^6 \nu^4 - 21 b \beta^4 \mu^8 \nu^4 - 63 b \beta^4 \mu^2 \nu^6 + 189 b \beta^4 \mu^4 \nu^6 - \\
 & \left. 189 b \beta^4 \mu^6 \nu^6 + 63 b \beta^4 \mu^8 \nu^6 \right) \times 3/(448 b) \tag{32}
 \end{aligned}$$

where $\nu \equiv \cos \phi$. For comparison, in real space, the PT bispectrum is simply $B_{\text{eq}} = (12/7)[P_g(k)]^2$ (Fry 1984). The bottom left panel in Fig. 1 shows the ratio of the redshift- and real-space equilateral bispectra in

leading order PT, $A_B \equiv B_{s \text{ eq}}(\mu, \nu)/B_{\text{eq}}$. For $\mu = 0$ and $\phi = \pi/2$, the triangle lies in the plane perpendicular to the line-of-sight, and there are no redshift distortions ($A_B = 1$). The maximum distortion occurs for $\mu = 0$, $\phi = \pi$, with an enhancement factor $A_B = 189/48 = 3.94$. A similar enhancement ($A_B = 1005/256 = 3.93$) is obtained for the configuration with $\mu = 1$, independent of ϕ .

Averaging over ϕ , the equilateral redshift-space bispectrum becomes

$$\begin{aligned}
 B_{s \text{ eq}}(\mu) = & [P_g(k)]^2 \left(4096 + 2304\beta + 1792b\beta + 432\beta^2 + 1008b\beta^2 + 7168\gamma + 3584\beta\gamma + 504\beta^2\gamma + \right. \\
 & 2304\beta\mu^2 + 1792b\beta\mu^2 + 288\beta^2\mu^2 + 672b\beta^2\mu^2 + 216\beta^3\mu^2 - 315b\beta^4\mu^2 + 3584\beta\gamma\mu^2 + \\
 & 336\beta^2\gamma\mu^2 + 432\beta^2\mu^4 + 1008b\beta^2\mu^4 - 624\beta^3\mu^4 + 819b\beta^4\mu^4 + 504\beta^2\gamma\mu^4 + \\
 & \left. 472\beta^3\mu^6 - 413b\beta^4\mu^6 - 203b\beta^4\mu^8 \right) \times 3/(7168b)
 \end{aligned} \tag{33}$$

Decomposing into Legendre polynomials, $B_{s \text{ eq}}(\mu) = \sum_{\ell=0}^{\infty} B_{s \text{ eq}}^{(\ell)} P_{\ell}(\mu)$, and defining the equilateral hierarchical amplitude in redshift-space, $Q_{s \text{ eq}}^{(\ell=0)} \equiv B_{s \text{ eq}}^{(\ell=0)}/3[P_s(k)]^2$, we obtain

$$Q_{s \text{ eq}}^{(\ell=0)} = \frac{5(2520 + 4410\gamma + 1890\beta + 2940\gamma\beta + 378\beta^2 + 441\gamma\beta^2 + 9\beta^3 + 1470b\beta + 882b\beta^2 - 14b\beta^4)}{98b(15 + 10\beta + 3\beta^2)^2}. \tag{34}$$

This result shows once again that in redshift space, $Q_{s,g} \neq (Q_s + \gamma)/b$ (although, as shown in Fig. 1, it is not a bad approximation). In the absence of bias ($b = 1$, $\gamma = 0$), Eq. (34) yields

$$Q_{s \text{ eq}}^{(\ell=0)} = \frac{5(2520 + 3360f + 1260f^2 + 9f^3 - 14f^4)}{98(15 + 10f + 3f^2)^2}, \tag{35}$$

which approaches the real-space result $Q_{\text{eq}} = 4/7 = 0.57$ in the limit $f \sim \Omega^{0.6} \rightarrow 0$. On the other hand, for $f = \Omega = 1$, we have $Q_{s \text{ eq}}^{(0)} = 0.464$: for these configurations, the hierarchical 3-point amplitude is suppressed by redshift distortions. For the quadrupole-to-monopole ratio of B_{eq} we have

$$R_{B \text{ eq}} = \frac{5(4158\beta + 3234\gamma\beta + 1188\beta^2 + 693\gamma\beta^2 + 33\beta^3 + 3234b\beta + 2772b\beta^2 - 56b\beta^4)}{22(2520 + 4410\gamma + 1890\beta + 2940\gamma\beta + 378\beta^2 + 441\gamma\beta^2 + 9\beta^3 + 1470b\beta + 882b\beta^2 - 14b\beta^4)}. \tag{36}$$

For no bias and $\Omega = 1$, this gives $R_{B \text{ eq}} = 11329/31394 = 0.36$. Eqs. (34-36) provide two constraints upon (b, β, γ) that are independent of the power spectrum. Thus, these relations for $Q_{s \text{ eq}}^{(\ell=0)}$ and $R_{B \text{ eq}}$, together with the power spectrum quadrupole-to-monopole ratio R_P from Eq. (15), could in principle be inverted to obtain Ω , b , and b_2 at large scales, independent of the initial conditions. In practice, R_P will determine β , while $Q_{s \text{ eq}}^{(\ell=0)}$ and $R_{B \text{ eq}}$ then constrain the b, γ parameter space. Moreover, R_B is very insensitive to b and only mildly sensitive to γ , so that there will typically be some residual degeneracy between b and γ . To break this degeneracy, one could use the shape-dependence of B , i.e., non-equilateral configurations (Fry 1994).

4. Results: The Redshift-Space Bispectrum in Numerical Simulations

4.1. Numerical Simulations

The numerical simulations used in this work correspond to cluster-normalized cold dark matter (CDM) models run by the Virgo collaboration (see e.g., Jenkins et al. 1998 for more details). We present results for standard CDM (hereafter SCDM, with $\Omega = 1$, $h = 0.5$) and “Lambda” CDM (hereafter Λ CDM, with $\Omega = 0.3$, $\Omega_\Lambda = 0.7$, $h = 0.7$), although we have also done measurements in τ CDM ($\Omega = 1$ with power spectrum shape parameter $\Gamma = 0.21$) and open CDM ($\Omega = 0.3$, $h = 0.7$) models. We found the results for SCDM and Λ CDM to be representative of the full set of simulations. These simulations each contain 256^3 particles in a box $240h^{-1}$ Mpc on a side. They were run with an adaptive P³M code (Couchman, Thomas & Pearce, 1995; Pearce & Couchman, 1997), and the initial conditions were set using the Zel’dovich approximation on a “glass” (see, e.g. White 1996). We have also made measurements in a set of smaller simulations run by the Hydra Consortium (Couchman, Thomas & Pearce, 1995), with very similar results.

We use the plane-parallel approximation to construct the redshift-space maps, so that the periodic boundary conditions in the simulation box are preserved by the redshift-space mapping. We can therefore continue to use the FFT to obtain the density field in Fourier space. This also has the advantage that our N-body measurements are done using the same approximation as our perturbative calculations. We consider four different observer’s directions, in all cases misaligned with respect to the simulation box sides to avoid spurious effects. Error bars in the plots denote the dispersion in the values obtained for these four observers. To measure the bispectrum in the numerical simulations, we use the method described in Scoccimarro et al. (1998), developed by S. Colombi, with minor improvements such as using TSC instead CIC to do the interpolations.

4.2. Phenomenological Description of Non-Linear Redshift Distortions

In order to describe the non-linear behavior of the redshift-space bispectrum, we introduce a phenomenological model to take into account the velocity dispersion effects and to quantify their importance. We follow the standard approach in the literature (Peacock & Dodds 1994), in which the non-linear distortions of the power spectrum in redshift-space are written in terms of the linear squashing factor and a suitable damping factor due to the pairwise-velocity distribution function

$$P_s(\mathbf{k}) = P_g(k) \frac{(1 + \beta\mu^2)^2}{[1 + (k\mu\sigma_v)^2/2]^2} . \quad (37)$$

Here σ_v is a free parameter that characterizes the velocity dispersion along the line-of-sight. This Lorentzian form of the damping factor is motivated by empirical results showing an exponential one-particle velocity distribution function (Park et al. 1994); comparison with N-body simulations have shown it to be the best phenomenological model so far (Cole, Fisher & Weinberg 1995; Hatton & Cole 1998). It is straightforward to obtain the multipole moments of $P_s(\mathbf{k})$ in this simple model (Cole, Fisher & Weinberg 1995). In comparing with numerical simulations, we use the quadrupole-to-monopole ratio statistic $R_P = a_2/a_0$ to fit σ_v .

We propose a similar ansatz to model non-linear distortions of the bispectrum:

$$B_s(\mathbf{k}_1, \mathbf{k}_2, \mathbf{k}_3) = \frac{B_s^{\text{PT}}(\mathbf{k}_1, \mathbf{k}_2, \mathbf{k}_3)}{[1 + \alpha^2 [(k_1\mu_1)^2 + (k_2\mu_2)^2 + (k_3\mu_3)^2]^2 \sigma_v^2/2]^2}, \quad (38)$$

where $B_s^{\text{PT}}(\mathbf{k}_1, \mathbf{k}_2, \mathbf{k}_3)$ is the tree-level redshift-space bispectrum derived in the last section. Note that we

have written the triplet velocity dispersion along the line-of-sight in terms of the pairwise velocity dispersion parameter σ_v and a constant α which reflects the configuration dependence of the triplet velocity dispersion. As noted above, σ_v is determined from simulations solely using the power spectrum ratio R_P ; the parameter α is then fitted by comparison with the monopole-to-quadrupole ratio of the equilateral bispectrum, R_B , measured in the simulations. The simpler phenomenological model in which the suppression factor in the denominator in Eq. (38) is replaced by $1 + [(k_1\mu_1)^2 + (k_2\mu_2)^2 + (k_3\mu_3)^2]\sigma_v^2/2$ does well in comparison with the N-body results for configurations where $k_2/k_1 = 2$, but does not reproduce the results of the equilateral quadrupole-to-monopole ratio R_B . In what follows we find good fits to the measured bispectrum using $\alpha \simeq 2$ for equilateral configurations and $\alpha \simeq 3$ for $k_1/k_2 = 2$ configurations, independent of cosmology (at redshift $z = 0$). For $z = 1$, we find that $\alpha = 1$ (SCDM) and $\alpha = 1.75$ (Λ CDM) reproduce the shape of R_B . This is similar to the modelling of the equilateral three-point function by Matsubara (1994), who found it necessary to have a triplet velocity dispersion parameter $\sigma_3 \approx 1.7\sigma_v$ to fit the N-body simulations. We note here that we have not attempted to do any best-fit procedure to obtain σ_v and α : these values were simply obtained by inspecting by eye the results for R_P and the bispectrum. We also note that eqn. (38) reduces to the perturbative expression B_s^{PT} at large scales ($k \rightarrow 0$), so it has the correct limiting behavior [e.g. Eqs. (34-36)].

4.3. Comparison with Numerical Simulations

Figure 2 shows the results from the phenomenological redshift-distortion model and how it compares with N-body simulations. Error bars have been suppressed for clarity but can be guessed from the dispersion of the data points. For the SCDM model, from R_P we obtain $\sigma_v = 6$ (in units of $H_0=100 h \text{ km/s/Mpc}$) for $z = 0$ and $\sigma_v = 2$ for $z = 1$. Using this result, we can predict the equilateral bispectrum ratio R_B in the phenomenological model by taking multipoles of Eq. (38). The results are shown as the solid curves in Fig. 2, showing excellent agreement with the N-body simulations. Similarly, for the Λ CDM model, from fitting R_P we obtain $\sigma_v = 5.5$ for $z = 0$ and $\sigma_v = 4$ for $z = 1$. The results for R_B are again in very good agreement with the numerical simulations. Note the similar behavior of R_P and R_B as a function of scale: the FOG effect, which creates a deficit of pairs along the line-of-sight, also causes a decrease of triplets compared to those in the perpendicular direction. In this sense, it is a reassuring check to note that in every case the zero-crossings of R_P and R_B are very close to each other in scale.

The top left panel of Fig. 3 shows the power spectrum amplitude $\Delta(k) = 4\pi k^3 P(k)$ in real (squares) and redshift (triangles) space for SCDM, with the corresponding linear theory predictions. In the figures, perturbative predictions are denoted by ‘‘PT’’ (real space) and ‘‘PTs’’ (redshift space). At large scales, the squashing effect boosts the power (Kaiser 1987), whereas at small scales the FOG effect erases power in the monopole of the power spectrum. The top right panel shows the equilateral hierarchical amplitude Q in real (squares) and redshift (triangles) space, with the corresponding predictions of tree-level PT given by Eq. (35) in redshift space and $Q_{\text{eq}} = 4/7$ in real space. Note the similarity to the power spectrum results: at small scales the FOG effect maintains the redshift-space equilateral amplitude close to its perturbative value, while in real space the amplitude grows by a large factor. This result, or the analog of this result for the skewness $S_3(R)$ (i.e., the fact that S_3 in redshift space is less scale-dependent than in real space), has led previous authors to conclude that higher-order correlations are ‘more hierarchical’ in redshift-space than in real space (Lahav et al. 1993; Matsubara 1994, Matsubara and Suto 1994; Suto and Matsubara 1994; Bonometto et al. 1995; Ghigna et al. 1996). However, this interpretation is in fact not correct: the FOG effect at small scales decreases the equilateral amplitude with respect to the real space value and shifts power to the co-linear

configurations. Therefore a strong configuration dependence of the bispectrum is expected in redshift space, even when the real-space correlations are well described by the hierarchical model (Scoccimarro et al. 1998). This is exactly what we find in numerical simulations (bottom right panels in Figs. 3 and 4), and what the model in Eq. (38) predicts.

The bottom panels in Fig. 3 show a comparison of simulations to the predictions of PT and the phenomenological model of Eq. (38) for configurations with $k_2/k_1 = 2$, for two different scales: $k_1 = 10 k_f$ (left) and $k_1 = 20 k_f$ (right), where the fundamental wavenumber of the simulation box is $k_f = 2\pi/240 h\text{Mpc}^{-1}$. In the bottom left panel, where the amplitude $\langle \Delta \rangle \approx \Delta(k_2) = 2.5$ (thus somewhat beyond the weakly non-linear regime), the tree-level PT calculation in real space (dashed curve) predicts the form of the N-body results for Q reasonably well, although not to high accuracy. However, the redshift-space PT counterpart (dotted curve) does not provide a good description of the simulation results for Q_s . This illustrates the point that PT tends to break down on larger scales in redshift space than in real space. On the other hand, the phenomenological model of Eq. (38) (solid curve) describes the N-body results for Q_s very well. If one were instead to use the redshift-space PT prediction [Eq. (21)] at these scales to probe the bias, one would mistakenly conclude that the bias is $b = 1.7$ instead of 1.

A similar set of plots is shown in Figure 4 for the ΛCDM model, corresponding to $k_1/k_f = 5, 10, 20$. Even at the largest scale probed, corresponding to a wavelength $\lambda \simeq 50 \text{ Mpc}/h$, the tree-level PT prediction in redshift space is a poor fit to the simulation results; using it, one would erroneously predict an effective bias $b = 1.4$, a quite significant discrepancy. The bottom right panel nicely illustrates our point about correlations in the strongly non-linear regime: whereas Q is very close to hierarchical (nearly configuration- and scale-independent), the redshift-space amplitude Q_s displays a strong configuration dependence. The phenomenological model (solid curve) does an excellent job in predicting Q_s , even at this stage of considerable non-linearity.

In a recent paper, Verde et al. (1998) independently proposed a somewhat different phenomenological model to take into account redshift-space distortions of the bispectrum, $\delta_s(\mathbf{k}) = \delta_s^{\text{PT}}(\mathbf{k})/\sqrt{1 + (k\mu\sigma_v)^2/2}$, which makes their damping factor in Eq. (37) the square root of ours. We find that the resulting power spectrum quadrupole-to-monopole ratio R_P does not have the correct shape when compared to numerical simulations, although it can be made to fit the low- k behavior. If we fit σ_v to the simulation R_P using their model, we find that the predicted $Q_s^{(l=0)}$ does not provide a very accurate fit to the simulation results. In particular, comparing their model to the simulation results in Figs. 3 (bottom left) and 4 (top right) would lead one to erroneously conclude that there is an effective bias of $b = 1.5$ and $b = 1.4$, respectively.

The Verde et al. phenomenological model can however be improved as follows (Heavens 1998, private communication). The power spectrum quadrupole-to-monopole ratio can be fixed by introducing a scale dependence of the velocity dispersion parameter $\sigma_v \rightarrow \sigma_v(k)$. Furthermore, using the non-linear power spectrum in the perturbative formula for the bispectrum, Eq. (16), and removing the wavevectors close to the line of sight leads to Q_s values that agree with numerical simulations. However, this statistic is not exactly equal to the monopole average $Q_s^{(l=0)}$, since some configurations are not included in the averaging procedure. We conclude, therefore, that the phenomenological model of Eq. (38) is the simplest way to accurately extract bias parameters from redshift-space data.

5. Conclusions and Discussion

We have derived the fully non-linear expression for the density field in redshift space in the plane-parallel approximation and applied this result to obtain the redshift-space bispectrum to leading order in PT. This derivation in Eulerian space is both simple and transparent and can in fact be extended beyond leading order to understand the large-scale FOG effect from a dynamical point of view (SCF). We computed the multipole expansion of the bispectrum in redshift space, in particular the monopole (Hivon et al. 1995) and quadrupole, including the effects of non-linear biasing. These perturbative results provide in principle a means of breaking the degeneracy between bias and Ω present in measurements of the redshift-space power spectrum on large scales.

We found that, even at relatively large scales (e.g., $50 h^{-1}\text{Mpc}$) the leading-order PT predictions in redshift space are not accurate enough for detailed modelling and can lead to systematic errors in the determination of the bias. This is similar to what happens with the power spectrum: redshift-space statistics are more strongly affected by non-linearities than their real-space counterparts. In this respect, it is interesting to note that even in the linear dynamics, the exponential factor in Eq. (4) can lead to a FOG effect at large scales (SCF). Therefore, the long range of the FOG effect seen in numerical simulations, should not be attributed exclusively to virialized clusters. This behavior agrees with the results of Taylor & Hamilton (1996) and Fisher & Nusser (1996), who found that they could qualitatively reproduce the shape of R_p seen in numerical simulations by using the Zel’dovich approximation, although quantitatively its use can lead to systematic errors (Hatton & Cole 1998). The large-scale FOG effect has been recently connected to redshift-space shell-crossing due to coherent infall by Hui, Kofman & Shandarin (1998). All of these results strongly suggest the possibility of extending the leading-order PT results for the power spectrum and bispectrum to smaller scales by treating the redshift-space mapping in Eq. (4) exactly and approximating the dynamics using PT (SCF).

To correct for these non-linear effects, we have developed a phenomenological model that convolves the PT results with a damping factor due to velocity dispersion. Comparison with high-resolution numerical simulations shows that this model, calibrated using the power spectrum distortions, works very well and provides a quantitative tool that can be applied to galaxy redshift surveys.

In the strongly non-linear regime, the reduced bispectrum is very close to hierarchical (configuration-independent) in real space. However, in redshift space we found that there is a strong configuration dependence that reflects the velocity dispersion of clusters. This helps to understand the deviations from the hierarchical ansatz reported recently in the LCRS redshift-survey three-point function (Jing & Börner 1998). For equilateral configurations, on the other hand, the FOG effect suppresses the scale-dependence of $Q_{s\text{ eq}}$ compared to that of Q_{eq} , and this can be misinterpreted as a sign of hierarchical correlations in redshift space. A similar effect occurs with the skewness factor S_3 , which in redshift space shows a remarkable scale-independence from weakly non-linear scales into the non-linear regime (Hivon et al. 1995). Although Q_{eq} and S_3 in redshift space remain very close to their PT values well into the non-linear regime, one must be careful using the standard non-linear biasing prescriptions beyond the regime of validity of tree-level PT, since non-commutativity of redshift distortions and biasing may be more complex than that exhibited at large scales.

We thank E. Bertschinger, S. Colombi, J. Fry, A. Hamilton, A. Heavens, L. Hui, R. Juszkiewicz, D. Pogosyan, L. Verde, and D. Weinberg for useful discussions. HMPC thanks CITA for hospitality during 1996–7 and frequent subsequent visits. The numerical simulations analyzed in this paper were carried out by the Virgo Supercomputing Consortium (<http://star-www.dur.ac.uk/~frazierp/virgo/virgo.html>) using computers based at the Max Plank Institut fur Astrophysik, Garching and the Edinburgh Parallel Computing Centre.

REFERENCES

- Bonometto, S. A., Borgani, S., Ghigna, S., Klypin, A., & Primack, J. R. 1995, *MNRAS*, 273, 101
- Cole, S., Fisher, K. B., & Weinberg, D. 1994, *MNRAS*, 267, 785
- Cole, S., Fisher, K. B., & Weinberg, D. 1995, *MNRAS*, 275, 515
- Couchman, H. M. P., Thomas, P. A., & Pearce, F. R. 1995, *ApJ*, 452, 797
- Fisher, K., & Nusser, A., 1996, *MNRAS*, 279, L1
- Fry, J. N. 1984, *ApJ*, 279, 499
- Fry, J. N. 1994, *Phys. Rev. Lett.*, 73, 215
- Fry, J. N. & Gaztañaga, E. 1993, *ApJ*, 413, 447
- Gaztañaga, E. & Frieman, J. A. 1994, *ApJ*, 437, L13
- Ghigna, S., Bonometto, S. A., Guzzo, L., Giovanelli, R., Haynes, M. P., Klypin, A., Primack, J. R. 1996, *ApJ*, 463, 395
- Goroff, M. H., Grinstein, B., Rey, S.-J., & Wise, M. 1986, *ApJ*, 311, 6
- Hamilton, A. J. S. 1992, *ApJ*, 385, L5
- Hamilton, A. J. S. 1997, in *Proceedings of Ringberg Workshop on Large-Scale Structure*, Hamilton, D. (ed.), Kluwer Academic, Dordrecht, *astro-ph/9708102*.
- Hatton, S., & Cole, S., 1998, *MNRAS*, 296, 10
- Hivon, E., Bouchet, F. R., Colombi, S., & Juszkiewicz, R. 1995, *A&A*, 298, 643
- Hui, L., Kofman, L., & Shandarin, S.F. 1998, in preparation.
- Jackson, J.C. 1972, *MNRAS*, 156, 1P
- Jenkins, A. R., Frenk, C. S., Pearce, F. R., Thomas, P. A., Colberg, J. M., White, S. D. M., Couchman, H. M. P., Peacock, J. A., Efstathiou, G. P., & Nelson, A. H. 1998, *ApJ* 499, 20
- Jing, Y. P., & Börner, G. 1998, *astro-ph/9802011*.
- Kaiser, N. 1987, *MNRAS*, 227, 1
- Lahav, O., Itoh, M., Inagaki, S., & Suto, Y. 1993, *ApJ*, 402, 387
- Matarrese, S., Verde, L., & Heavens, A.F. 1997, *MNRAS*, 290, 651
- Matsubara, T. 1994, *ApJ*, 424, 30
- Matsubara, T., & Suto, Y. 1994, *ApJ*, 420, 497
- McGill, C. 1990, *MNRAS*, 242, 428
- Park, C., Vogeley, M. S., Geller, M. J., & Huchra, J. P. 1994, *ApJ*, 431, 569

- Peacock, J. A. & Dodds, S. J. 1994, MNRAS, 267, 1020
- Pearce F. R. & Couchman, H. M. P. 1997, New Astronomy, 2, 411
- Sargent, W.L., & Turner, E.L. 1977, ApJ212, L3
- Scoccimarro R., Colombi, S., Fry, J. N., Frieman, J., Hivon, E., & Melott, A., 1998, ApJ, 496, 586
- Scoccimarro R., Couchman, H. M. P., & Frieman, J. 1998, in preparation (SCF)
- Suto, Y., & Matsubara, T. 1994, ApJ, 420, 504
- Taylor, A. N., & Hamilton, A. J. S., 1996, MNRAS, 282, 767
- Verde, L., Heavens, A.F., Matarrese, S., & Moscardini, L. 1998, astro-ph/9806028.
- White, S. D. M. 1996, in Cosmology and Large-Scale Structure, eds. Schaeffer, R., Silk, J., Spiro, M., & Zinn-Justin, J., Elsevier, 349.

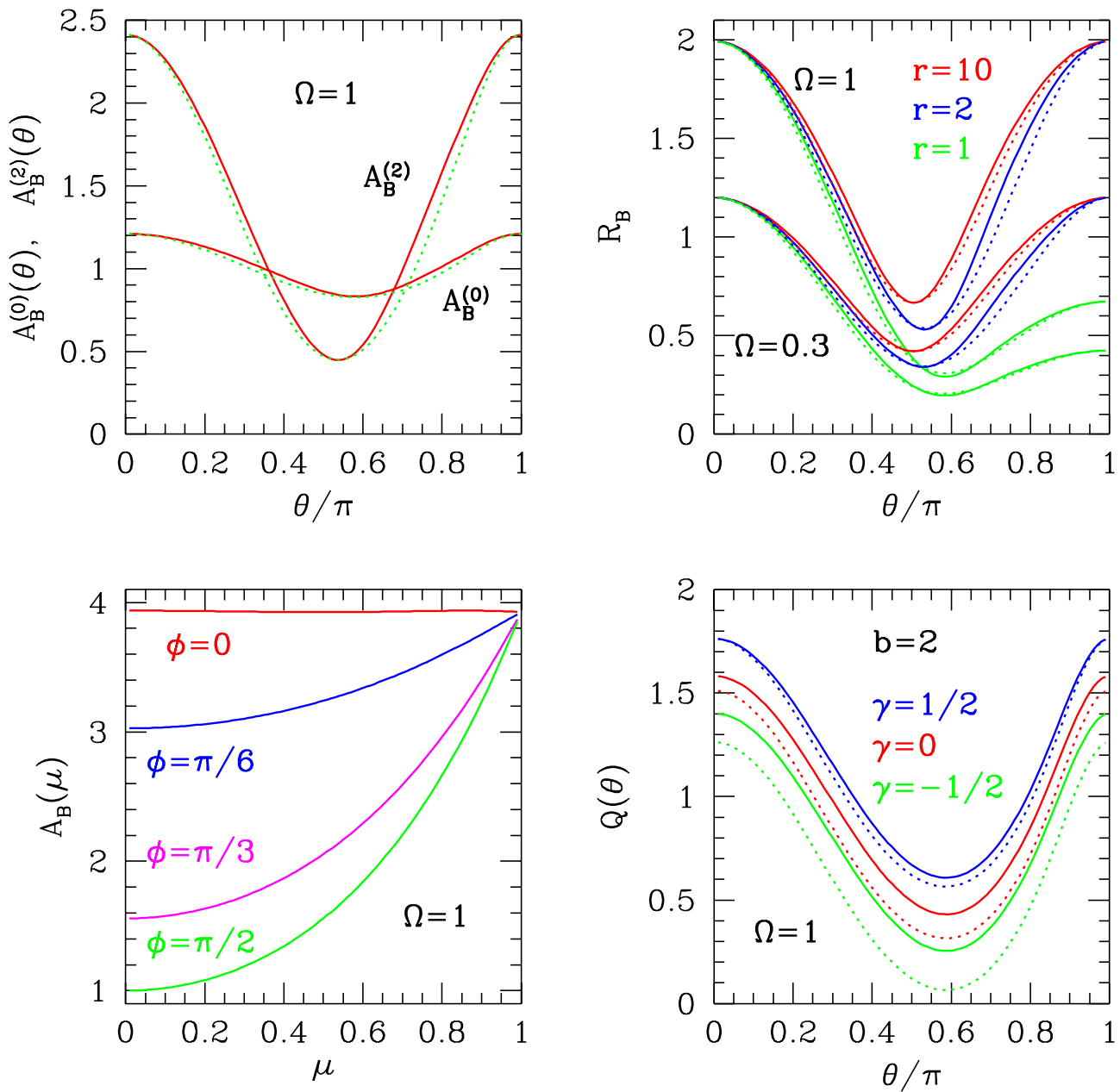


Fig. 1.— Top left panel shows the redshift-space tree-level bispectrum multipoles, $A_B^{(\ell)} \equiv B_s^{(\ell)}/B$, as a function of angle $\theta = \cos^{-1} \hat{k}_1 \cdot \hat{k}_2$, for configurations with $k_1/k_2 = 2$ and scale-free initial spectra, $P(k) \propto k^n$ ($n = -2$ solid, $n = 0$ dotted). Top right panel shows the bispectrum quadrupole-to-monopole ratio $R_B = B_s^{(2)}/B_s^{(0)}$ for $r = k_1/k_2 = 10, 2, 1$ configurations as a function of θ ($n = -2$ solid, $n = 0$ dotted) for $\Omega = 1$ and $\Omega = 0.3$. The bottom left plot shows the ratio of the redshift-space to real-space bispectrum for equilateral triangles, as a function of $\mu = \hat{k}_1 \cdot \hat{z}$ for different azimuthal angles ϕ . The bottom right plot shows the hierarchical amplitude Q_s for $k_1/k_2 = 2$ configurations with linear bias $b = 2$, and quadratic bias $\gamma = b_2/b = 1/2, 0, -1/2$ (top to bottom), for $n = -2$. Solid curves represent the PT result, and dotted curves assume that bias and redshift-space mapping commute.

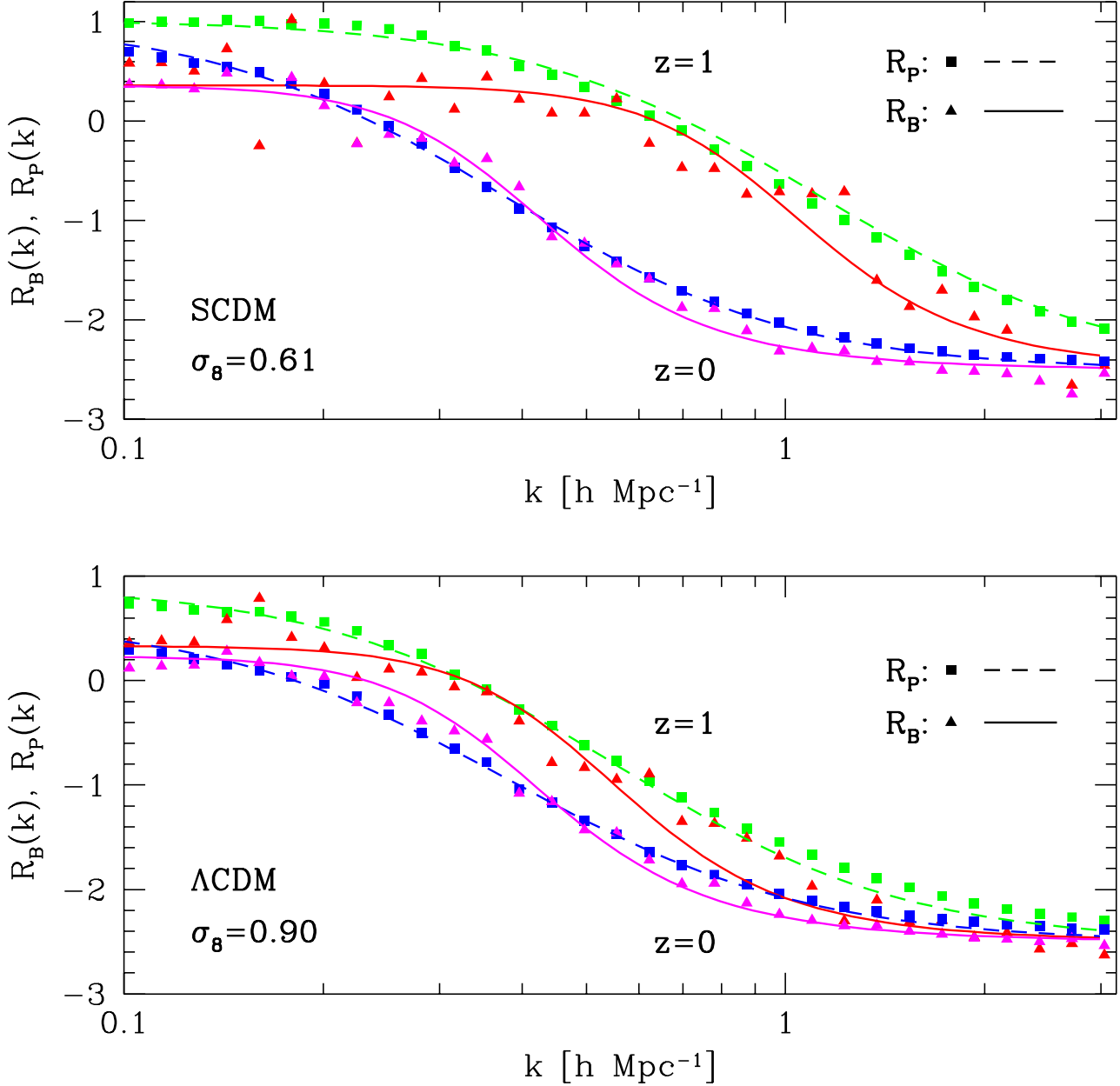


Fig. 2.— The quadrupole-to-monopole ratio for the redshift-space power spectrum, R_P , and equilateral bispectrum, R_B . The symbols correspond to AP³M 256³ particle N-body simulations (see text) at redshift $z = 0, 1$ averaged over four different observers, for SCDM (top) and Λ CDM (bottom). Squares denote measured values of R_P , and triangles correspond to values of the ratio R_B . The dashed and solid curves show the predictions of PT convolved with an exponential velocity dispersion model, Eqs. (37-38).

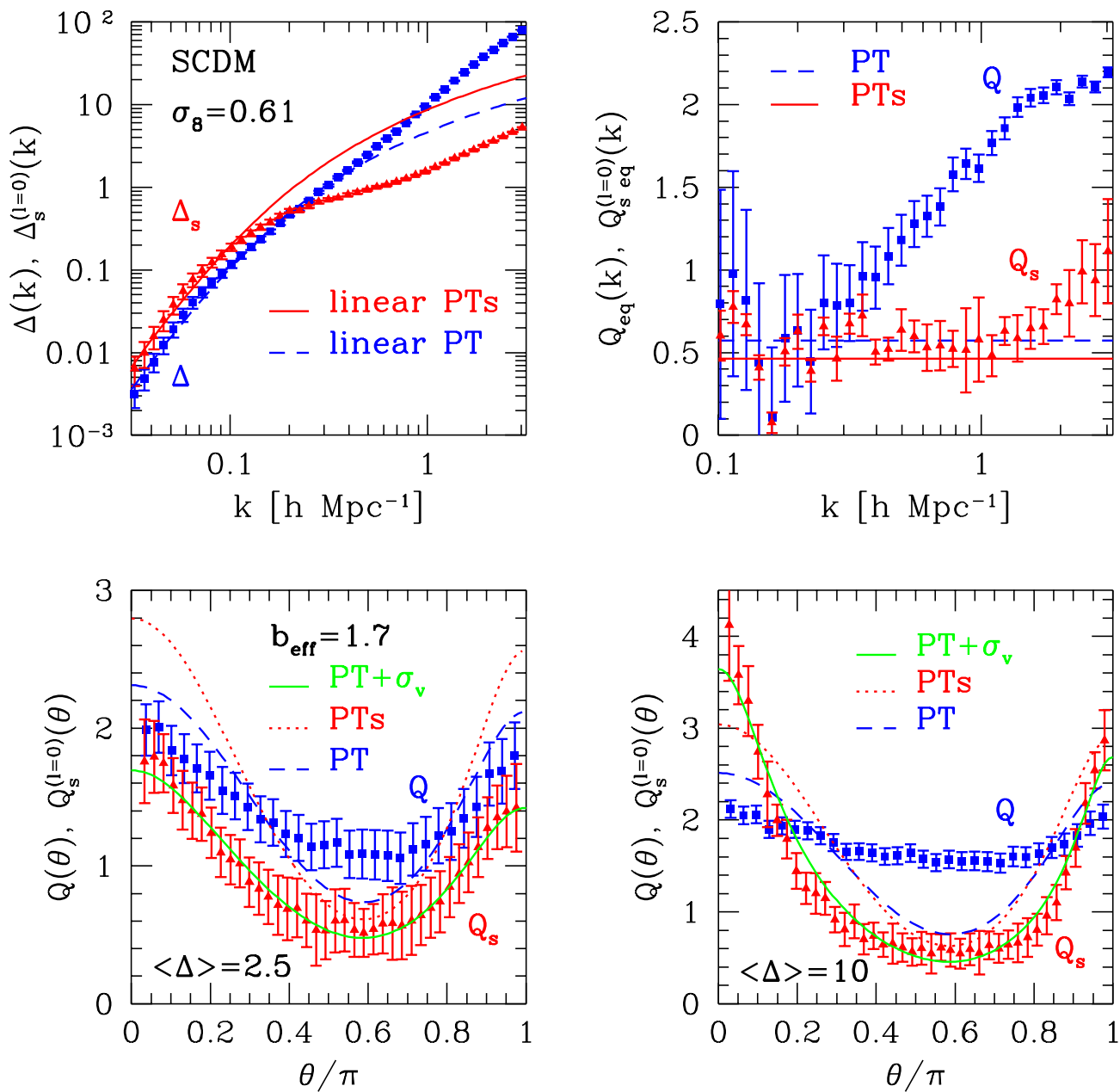


Fig. 3.— The top left panel shows the power spectrum amplitude, $\Delta(k) \equiv 4\pi k^3 P(k)$ in real (squares) and redshift (triangles) space. The top right panel shows the equilateral hierarchical amplitude Q_{eq} in real-space (squares) and the monopole of the redshift-space amplitude, $Q_{s \text{ eq}}$ (triangles). The bottom panels show the hierarchical amplitude Q for $k_2/k_1 = 2$ configurations, as a function of the angle θ between \mathbf{k}_1 and \mathbf{k}_2 , in real (squares) and redshift space (triangles), for two different scales. In the bottom left plot, weakly non-linear distortions decrease the configuration dependence of Q_s , similar to the effects of bias in leading order PT. At smaller scales (lower right panel), the configuration dependence of Q_s is greatly enhanced, reflecting the velocity dispersion of virialized clusters.

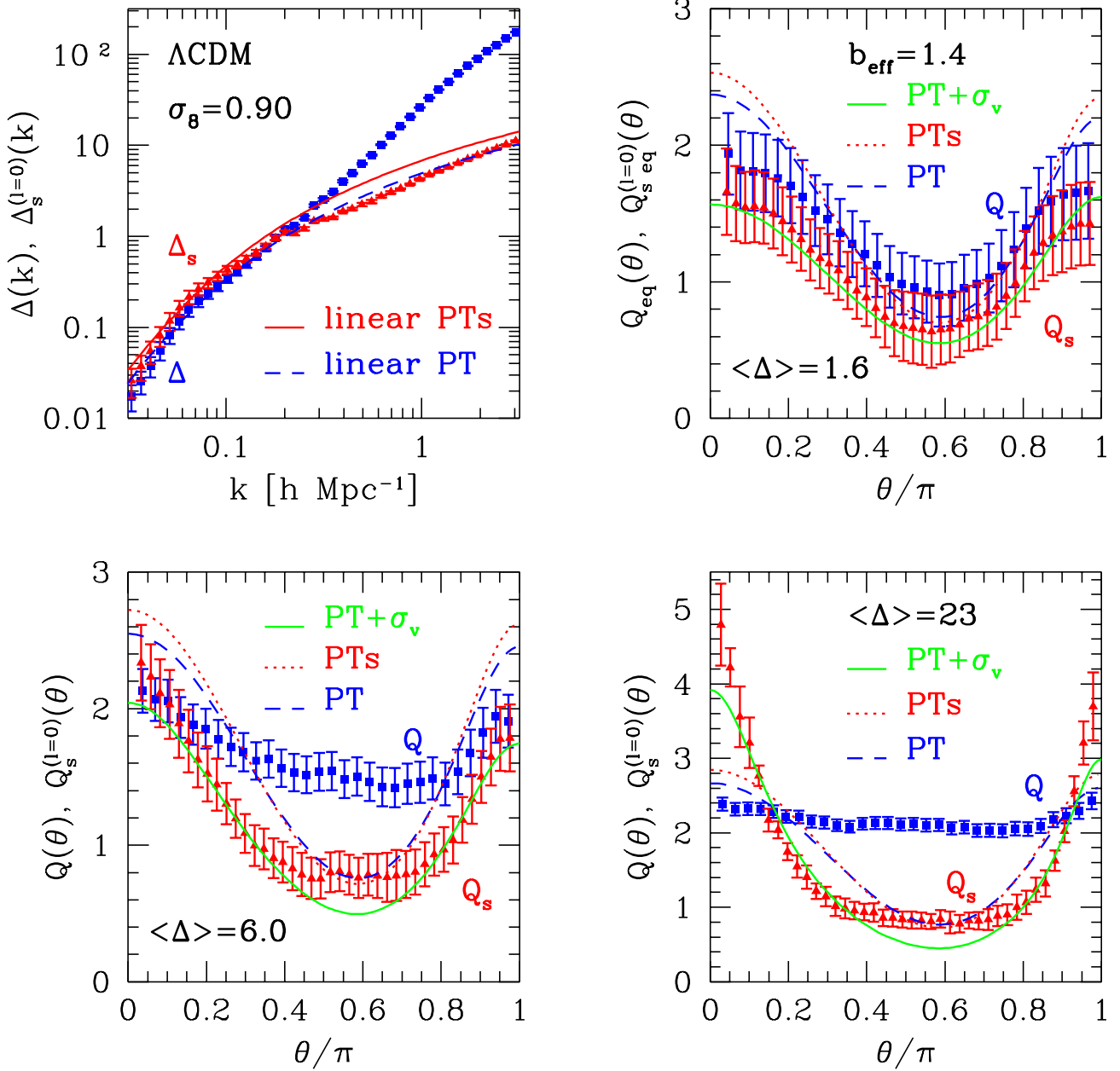


Fig. 4.— Same as Fig 3, for the Λ CDM model. In the bottom right panel note the difference between the real- and redshift-space hierarchical amplitudes. Whereas Q in real-space is approximately constant, its redshift-space counterpart depends strongly on configuration. Therefore, the hierarchical ansatz does not hold in redshift space.